V. Conclusion

A neural network-based synthesis method able to obtain the voltages that must be applied to the elements of a given array taking into account coupling effects between elements and the presence of a conducting obstacle in a near environment (or any element with influence over the radiated field distribution) has been presented. This method outputs valid solutions in problems that cannot even be considered with traditional synthesis methods, allowing the accurate design of adaptive antennas in complex environments. The synthesis process, with the presented technique, is performed without any increase of the complexity from the designer's point of view.

References

[1] H. Steyskal, "Synthesis of antenna patterns with imposed near-field nulls," *IEE Electron. Lett.*, vol. 30, no. 24, pp. 2000–2001, Nov. 1994.

[2] S. Haykin, *Neural Networks: A Comprehensive Foundation*. New York: Macmillan, 1994.

[3] A. H. El Zooghby, C. G. Christodoulou, and M. Georgiopoulos, "Neural network-based adaptive beamforming for one- and two-dimensional antenna arrays," *IEEE Trans. Antennas Propag.*, vol. 46, no. 12, pp. 1891–1893, Dec. 1998.

[4] ——, "A neural network-based smart antenna for multiple source tracking," *IEEE Trans. Antennas Propag.*, vol. 48, no. 5, pp. 768–776, May 2000.

[5] H. L. Southall, J. A. Simmers, and T. H. O'Donnell, "Direction finding in phased arrays with a neural network beamformer," *IEEE Trans. Antennas Propag.*, vol. 43, no. 12, pp. 1369–1374, Dec. 1995.

[6] A. H. El Zooghby, C. G. Christodoulou, and M. Georgiopoulos, "Performance of radial-basis function networks for direction of arrival estimation with antenna arrays," *IEEE Trans. Antennas Propag.*, vol. 45, no. 11, pp. 1611–1617, Nov. 1997.

[7] E. Carpentier and J. J. Laurin, "An implementation of a direction-finding antenna for mobile communications using a neural network," *IEEE Trans. Antennas Propag.*, vol. 47, no. 7, pp. 1152–1159, Jul. 1999.

[8] C. Christodoulou and M. Georgiopoulos, *Applications of Neural Networks in Electromagnetics*. Boston, MA: Artech House, 2001.

[9] J. C. Brégains, J. Dorado, M. Gestal, J. A. Rodríguez, F. Ares, and A. Pazos, "Avoiding interference in planar arrays through the use of artificial neural networks," *IEEE Antennas Propag. Mag.*, vol. 44, no. 4, pp. 61–65, Aug. 2002.

[10] R. G. Ayestarán and F. Las Heras, "Neural networks for the design of array antennas," in *Proc. Mediterranean Microwave Symp.*, Cáceres, Spain, Jun. 2002, pp. 193–196.

[11] ——, "Evaluation of array pattern synthesis methods based on artificial neural networks," in *Proc. Progress in Electromagnetic Research Symp.*, Boston, MA, Jul. 2002, p. 146.

[12] R. G. Ayestarán, F. Las Heras, and L. F. Herrán, "Neural network-based pattern synthesis of array antennas with element specification," in *Proc. IEEE Antennas and Propagation Symp.*, Monterey, CA, Jul. 2004, pp. 519–522.

[13] R. G. Ayestarán and F. Las Heras, "Neural networks and equivalent source reconstruction for real antenna array synthesis," *IEE Electron. Lett.*, vol. 39/13, no. 4, pp. 956–958, Jun. 2003.

[14] R. F. Harrington, *Field Computation by Moment Methods*. New York: Macmillan, 1968.

A PML Utilizing k-Vector Information as Applied to the Whistler Mode in a Magnetized Plasma

Michael W. Chevalier, Timothy W. Chevalier, and Umran S. Inan

***Abstract*—The perfectly matched layer (PML) in its most current form has shortcomings in certain cases involving propagation in anisotropic media, such as the whistler mode in a magnetized plasma, for which the vector component normal to the PML of the group velocity vector and the k-vector are anti-parallel with each other. We present a new type of PML that utilizes information on the k-vector direction by applying relevant spatial derivatives to the PML update equations. Derived expressions for the numerical reflection coefficient are used to quantify the performance of the PML for any incident angle. Numerical reflection calculations as well as time domain calculations are performed for whistler mode propagation in a magnetized plasma. We demonstrate the stability of the new PML and find that for the reflection coefficient Γ, values of up to –40 dB can be realized.**

***Index Terms*—Anisotropic, k-vector, perfectly matched layer (PML).**

I. Introduction

Since its introduction by Berenger [1] and Chew and Weedon [2] the perfectly matched layer (PML) has evolved to become the most effective absorbing boundary condition for the finite-difference time-domain (FDTD) technique as well as for other methods of numerical electromagnetic modeling. The original PMLs work well when the group and phase velocities of the incident wave are in the same direction. However, if these directions differ, as is the case for negative refractive index materials (NIMs) [3], [4] and certain electromagnetic propagation modes in magnetized plasmas, the regular PML ceases to attenuate the field and can in fact act as an amplifier. Becache *et al.* confirm this [5] with a theoretical analysis of PMLs for anisotropic media, for acoustic waves in elastic materials as well as electromagnetic waves. Their work is based on the split-field formulation [1]. Cummer [6] discusses the PML amplification phenomenon for NIMs in which the NIMs materials exhibits both positive and negative refractive indexes over a range of frequencies. He then derives a frequency dependent solution referred to as the NIMPML which is an adaptation of the previously introduced NPML [7].

Chevalier *et al.* [8] encounter the problems discussed in [5] when modeling the performance of an antenna in a magnetized plasma for waves in the whistler mode. In this paper, we discuss a PML which can be adapted to the direction of the group velocity as a function of frequency and k-vector direction. We then explicitly derive the PML equations for the whistler mode in a magnetized plasma with the ambient magnetic field perpendicular to the direction of the PML as discussed in [8]. We also derive expressions for the reflection coefficient and present numerical results for reflection coefficient calculations as well as time domain simulations.

Manuscript received August 19, 2005; revised March 16, 2006. This work was supported in part by the Air Force Office of Scientific Research (AFOSR) under Grant F49620-03-1-0338, and in part by the National Science Foundation under Grant OPP-0093381.

The authors are with the Space, Telecommunications, and Radioscience Laboratory, Department of Electrical Engineering, Stanford University, Stanford, CA 94305 USA (e-mail: chamonix@stanford.edu; timothyc@stanford.edu; inan@nova.stanford.edu).

Digital Object Identifier 10.1109/TAP.2006.879220

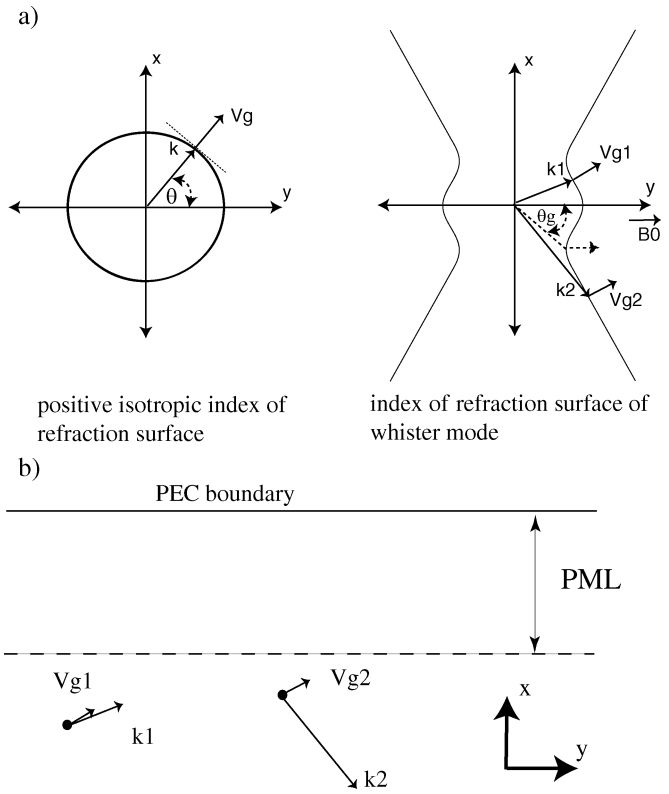

Fig. 1. (a) Index of refraction surfaces. (b) Two whistler waves incident on the PML [8].

II. A PML That Utilizes Information on the k-Vector Direction

We start with a brief review of the results of [5] and [6]. We discuss 2-D wave propagation in the xy plane only. We will assume $\vec{k} = k_x\hat{x} + k_y\hat{y}$ and $\vec{v}_g = v_{gx}\hat{x} + v_{gy}\hat{y}$, where $\vec{k}$ is the k-vector and $\vec{v}_g$ is the group velocity. This paper is concerned with the dot product of the x-directed components of $\vec{v}_g$ and $\vec{k}$, namely $v_{gx}k_x$. Fig. 1(a) displays two index of refraction surfaces [9] each at some chosen frequency. The direction of the vector from the origin to the index of refraction surface is the k-vector direction, i.e., the direction of the phase velocity. The direction of the vector that is normal to the index of refraction surface is the group velocity direction. The surface on the left is for a positive index of refraction, isotropic material, for which $v_{gx}k_x > 0$ always holds true. For the surface on the right hand side, which represents the whistler mode in a magnetized plasma, we see that $v_{gx1}k_{x1} > 0$ but $v_{gx2}k_{x2} < 0$. The so-called "Gendrin" angle [10], labeled Θ_g in Fig. 1(a), is the angle at which the whistler-mode index of refraction curve exhibits a minimum along the x-axis at two locations. The Gendrin angle is the non-zero k-vector angle at which the group velocity is along the ambient magnetic field and is the transition angle at which $v_{gx}k_x$ changes sign. The relationship for the Gendrin angle in a dense magnetized plasma is $cos(\Theta_g) \approx 2\omega/\omega_c$, where ω_c is the local electron gyro frequency. By dense plasma, we mean $\omega_c \ll \omega_p$, where ω_p is the local electron plasma frequency. We will only consider dense magnetized plasma. In the rest of the present paper we consider an x-directed PML only, unless otherwise noted. Fig. 1(b) shows an x-directed PML, i.e., only PML attenuation in the x-direction where the two examples $[\vec{v}_{g1}, \vec{k}_1]$ and $[\vec{v}_{g2}, \vec{k}_2]$ from the whistler index of refraction surface in Fig. 1(a) have been placed incident onto the PML region. In both cases, it is the group velocity in the x direction, "v_{gx}" that describes the speed in the $\hat{x}$-direction at which the wave energy is incident on the PML, but it is the k-vector in the x-direction, "k_x" that determines whether the PML amplifies or attenuates the wave. The x-directed wave solution within the PML region is

$$\begin{aligned}\text{solution form} : e^{-jk\left[\cos(\phi)x\left(1+\frac{\sigma_x}{j\omega}\right)\right]} &= e^{-jk\cos(\phi)x}e^{-\frac{\sigma_x k\cos(\phi)x}{\omega}} \\ &= e^{-jk_x x}e^{-\frac{\sigma_x k_x x}{\omega}}. \end{aligned} \tag{1}$$

For $v_{gx} > 0$, $k_x > 0$ the wave solution attenuates within the PML, i.e., the case for v_{gx1}, k_{x1}. For $v_{gx} > 0$, $k_x < 0$ the wave solution grows within the PML, i.e., the case for v_{gx2}, k_{x2}. We therefore need to somehow encode, $v_{gx}k_x$ into the PML, or at least encode the appropriate sign of $v_{gx}k_x$.

We define the incident k-vector as $\vec{k}_{inc} = k_x\hat{x} + k_y\hat{y}$ and the k-vector within the PML to be $\vec{k}_{\text{pml}} = k_{x_{\text{pml}}}\hat{x} + k_y\hat{y}$. Because of Snell's law and for an x-directed PML, k_y is preserved through the two mediums. We introduce the function, $f(\omega, k_{x_{\text{pml}}}, k_y)$. Focusing our attention to the x-directed portion of the PML wave solution we take it to be

$$\begin{aligned}\text{solution form} : e^{-jk_{x_{\text{pml}}}x} &= e^{-j\left(\kappa k_x x\left(1+\frac{\sigma_x f\left(\omega,k_{x_{\text{pml}}},k_y\right)}{j\omega}\right)\right)} \\ &= e^{-jk_x s_x x} \end{aligned} \tag{2}$$

where $f(\omega, k_{x_{\text{pml}}}, k_y) = 1$ would reduce to the original Berenger PML. The term κ is the tradition PML term for attenuating evanescent fields. In order for (2) to always have an attenuating solution we require that $f(\omega, k_{x_{\text{pml}}}, k_y)$ have the same sign as $v_{gx}k_x$. Equation (2) is similar to the formulation of [6], but we have additionally included k-vector direction information by including k-dependence explicitly in our PML attenuation function. We refer to this new PML as the "KPML," where "K" refers to the use of k-vector information. Considering the whistler mode in a magnetized plasma as an explicit example, ideally the function $f(\cdot)$ might be

$$\begin{aligned} f_{\text{ideal}}(\omega, k_x, k_y) &= k^2\left(cos^2(\Theta) - cos^2(\Theta_g)\right)\frac{1}{1-\frac{\omega_c^2}{\omega_0^2}} \\ &= \left(k_y^2 - \frac{4\omega^2}{\omega_c^2}\left[k_x^2 + k_y^2\right]\right)\frac{1}{1-\frac{\omega_c^2}{\omega_0^2}} \end{aligned} \tag{3}$$

where we define Θ as the angle w.r.t to the y-axis as well as the static magnetic field as in Fig. 1(a). The function $f_{\text{ideal}}(\cdot)$ has perfect transition through the "Gendrin" angle from positive to negative values following the sign of the quantity $v_{gx}k_x$. The term $1/(1-(\omega^2/\omega_0^2))$ is applied from [6] for generality and changes sign at $\omega = \omega_0$, where ω_0 is a user adjustable parameter. To ensure that $1/(1-(\omega^2/\omega_0^2))$ is positive over the frequency range of the whistler mode we enforces that $\omega_0 > \omega_c$. All this said, however, for actual implementation $f(\cdot)$ must have the form

$$f\left(\omega, k_{x_{\text{pml}}}, k_y\right) = \left(k_y^2 - \frac{4\omega^2}{\omega_c^2}\left[\left(\frac{k_{x_{\text{pml}}}}{\kappa}\right)^2 + k_y^2\right]\right)\frac{1}{1-\frac{\omega_c^2}{\omega_0^2}} \tag{4}$$

where we have simply replaced k_x, the x-directed k-vector in the magnetized plasma, from (3) with $k_{x_{\text{pml}}}/\kappa$, the x-directed k-vector within the PML. The reason that $f(\cdot)$ must necessarily be of the form in (4) is the fact that (4) can be implemented using linear differential equations, which we will show below. Whereas, for the ideal function, given by (3), it is not apparent how this can be done within the PML. Note that $k_{x_{\text{pml}}}$ is in general complex since it includes the PML losses as well as information about the incident wave, k_x. From (2) it can be shown

that $k_{x_{\rm pml}} = \kappa k_x x(1+\sigma_x f(\omega, k_{x_{\rm pml}}, k_y)/j\omega)$. As a result, $f(\cdot)$ is complex, and we therefore must apply it with care. Also, to clarify, in (4), the term $(k_{x_{\rm pml}}/\kappa)^2$ is this way because it removes the evanescent scaling factor κ from $k_{x_{\rm pml}}$ so that $k_{x_{\rm pml}}/\kappa$ more closely maps to k_x, especially as $\sigma_x \to 0$.

In the following, we derive the update equations for the implementation of (4), by applying the stretched coordinate form of [2] on our x-directed PML spatial operator to obtain the form:

$$\frac{1}{s_x}\frac{\partial}{\partial x} = \frac{\frac{1}{\kappa}}{1+\frac{\sigma_x f\left(\omega, k_{x_{\rm pml}}, k_y\right)}{j\omega}}\frac{\partial}{\partial x}. \tag{5}$$

Assuming $f(\omega, k_{x_{\rm pml}}, k_y)$ takes the form of (4), our PML spatial operator then becomes

$$\frac{1}{s_x}\frac{\partial}{\partial x} = \frac{\frac{1}{\kappa}}{1+\frac{\sigma_x\left(k_y^2-\frac{4\omega^2}{\omega_c^2}\left[\left(\frac{k_{x_{\rm pml}}}{\kappa}\right)^2+k_y^2\right]\right)\frac{1}{1-\frac{\omega^2}{\omega_0^2}}}{j\omega}}\frac{\partial}{\partial x}. \tag{6}$$

Since we exclusively consider plane wave analysis we have $(\partial/\partial x) \to -jk_{x_{\rm pml}}$. If we assume to operate on H_z and introduce the auxiliary variable, $\Psi_{H_z,x}$, we can rewrite (6) as

$$\frac{\frac{\left(-jk_{x_{\rm pml}}\right)}{\kappa}}{1+\frac{\sigma_x\left(k_y^2-\frac{4\omega^2}{\omega_c^2}\left[\left(\frac{k_{x_{\rm pml}}}{\kappa}\right)^2+k_y^2\right]\right)\frac{1}{1-\frac{\omega^2}{\omega_0^2}}}{j\omega}}H_z = \Psi_{H_z,x} \tag{7}$$

for which the most natural method of solution would be an auxiliary differential equation. After some manipulation and inverse transformation from k space we obtain

$$j\omega\frac{\partial H_z}{\kappa\partial x}+\frac{(j\omega)^3}{\omega_0^2}\frac{\partial H_z}{\kappa\partial x} = j\omega\Psi_{H_z,x}+\frac{(j\omega)^3}{\omega_0^2}\Psi_{H_z,x}-\sigma_x\frac{\partial^2}{\partial y^2} \times\Psi_{H_z,x}-\sigma_x\frac{4(j\omega)^2}{\omega_c^2}\left(\frac{\partial^2}{\kappa^2\partial x^2}\Psi_{H_z,x}+\frac{\partial^2}{\partial y^2}\Psi_{H_z,x}\right) \tag{8}$$

where we can then apply the inverse Fourier transform to yield the time domain equation

$$\frac{\partial}{\partial t}\frac{\partial H_z}{\kappa\partial x}+\frac{1}{\omega_0^2}\frac{\partial^3}{\partial t^3}\frac{\partial H_z}{\kappa\partial x} = \frac{\partial}{\partial t}\Psi_{H_z,x}+\frac{1}{\omega_0^2}\frac{\partial^3}{\partial t^3}\Psi_{H_z,x}-\sigma_x\frac{\partial^2}{\partial y^2} \times\Psi_{H_z,x}-\sigma_x\frac{4}{\omega_c^2}\left(\frac{\partial^4}{\partial t^2\kappa^2\partial x^2}\Psi_{H_z,x}+\frac{\partial^4}{\partial t^2\partial y^2}\Psi_{H_z,x}\right). \tag{9}$$

The important result in (8) and (9) is the use of spatial derivatives to gain information about the waves in the PML region, where we have tailored $f(\omega, k_{x_{\rm pml}}, k_y)$ such that it follows the sign of $v_{gx}k_x$. This procedure ensures that the PML attenuates all whistler mode waves within it.

Applying finite differences to the y-dependent spatial derivative terms yields

$$\frac{\partial^2}{\partial y^2}\Psi_{H_z,x} \Rightarrow \frac{\Psi_{H_z,x}|^{n+.5}_{i,j+1.5,k}-2\Psi_{H_z,x}|^{n+.5}_{i,j+.5,k}+\Psi_{H_z,x}|^{n+.5}_{i,j-.5,k}}{(\Delta y)^2} \tag{10}$$

and

$$\frac{\partial^4}{\partial t^2\partial y^2}\Psi_{H_z,x} \Rightarrow \frac{\Psi_{H_z,x}|^{n+.5}_{i,j+1.5,k}-2\Psi_{H_z,x}|^{n+.5}_{i,j+.5,k}+\Psi_{H_z,x}|^{n+.5}_{i,j-.5,k}}{(\Delta t)^2(\Delta y)^2} -2\frac{\Psi_{H_z,x}|^{n-.5}_{i,j+.5,k}-2\Psi_{H_z,x}|^{n-.5}_{i,j+.5,k}+\Psi_{H_z,x}|^{n-.5}_{i,j-.5,k}}{(\Delta t)^2(\Delta y)^2} +\frac{\Psi_{H_z,x}|^{n-1.5}_{i,j+1.5,k}-2\Psi_{H_z,x}|^{n-1.5}_{i,j+.5,k}+\Psi_{H_z,x}|^{n-1.5}_{i,j-.5,k}}{(\Delta t)^2(\Delta y)^2} \tag{11}$$

where we would apply finite differences to the x-dependent derivative terms in the same manner. Note that since we are updating the $\Psi_{H_z,x}$ variables to $n+.5$ these terms in (10), (11) are implicit because to update $\Psi_{H_z,x}$ at the timestep $n+.5$ requires information of the its nearest $\Psi_{H_z,x}$ neighbors at the timestep $n+.5$. The solution of the implicit equations are not difficult to solve, but are computationally more demanding. Note that the electric and magnetic fields can still be updated using explicit leap-frog equations. For algorithmic speed, we therefore would like an explicit method for updating this equation. We can approximate (10), (11) by shifting the $\Psi_{H_z,x}$ terms located at $i, j+1.5, k$ and $i, j-.5, k$ back one timestep yielding

$$\frac{\partial^2}{\partial y^2}\Psi_{H_z,x} \approx\Rightarrow \frac{\Psi_{H_z,x}|^{n-.5}_{i,j+1.5,k}-2\Psi_{H_z,x}|^{n+.5}_{i,j+.5,k}+\Psi_{H_z,x}|^{n-.5}_{i,j-.5,k}}{(\Delta y)^2} \tag{12}$$

and

$$\frac{\partial^4}{\partial t^2\partial y^2}\Psi_{H_z,x} \approx\Rightarrow \frac{\Psi_{H_z,x}|^{n-.5}_{i,j+1.5,k}-2\Psi_{H_z,x}|^{n+.5}_{i,j+.5,k}+\Psi_{H_z,x}|^{n-.5}_{i,j-.5,k}}{(\Delta t)^2(\Delta y)^2} -2\frac{\Psi_{H_z,x}|^{n-1.5}_{i,j+.5,k}-2\Psi_{H_z,x}|^{n-.5}_{i,j+.5,k}+\Psi_{H_z,x}|^{n-1.5}_{i,j-.5,k}}{(\Delta t)^2(\Delta y)^2} +\frac{\Psi_{H_z,x}|^{n-2.5}_{i,j+1.5,k}-2\Psi_{Ey,x}|^{n-1.5}_{i,j+.5,k}+\Psi_{H_z,x}|^{n-2.5}_{i,j-.5,k}}{(\Delta t)^2(\Delta y)^2}. \tag{13}$$

This method would also be applied to the x-dependent derivative terms. Solving (9) in this manner produces an explicit update equation with the only unknown variable being the $\Psi_{H_z,x}$ term located at $i, j+.5, k$ and at timestep $n+.5$. We examine both explicit and implicit time domain simulations in Section IV. Also, one can use (8) with the finite-difference frequency-domain (FDFD) method, however, numerical results for this are not presented in this paper.

III. Adapting the Numerical Reflection Coefficient for the KPML Equations

We now aim to quantify the performance of the x-directed KPML that is T cells thick. We make some substitutions in the CCO-PML refection coefficient derivation from [11] so that we can adapt it for the KPML. We take equation (24) from [11] and rewrite it is as

$$\bar{\varepsilon}\frac{e^{j\omega\Delta t}-1}{\Delta t}E_{yt}|^{n,\omega}_{i,j+.5,k}+J_{yt}|^{n+.5,\omega}_{i,j+.5,k} = \frac{1-e^{jk_z\Delta z}}{\Delta z}H_{xt}|^{n+.5,\omega}_{i,j+.5,k+.5}-\Psi_{H_z,x}|^{n+.5,\omega}_{i,j+.5,k} \tag{14}$$

where the derivation of the reflection coefficient from [11] assumes time harmonic form and Snell's Law requires spatial harmonic form in

the $\hat{y}$ and $\hat{z}$ directions due to plane wave incidence on the x-directed PML. For this system, (9) is then written as

$$\begin{aligned}
&\frac{1-e^{-j\omega\Delta t}}{\Delta t}\left(1+\frac{1+e^{-i2\omega\Delta t}-2e^{-i\omega\Delta t}}{\omega_0^2(\Delta t)^2}\right)\\
&\times\frac{H_{zt}|^{n+.5,\omega}_{i+.5,j+.5,k}-H_{zt}|^{n+.5,\omega}_{i-.5,j+.5,k}}{\kappa\Delta x}\\
&\quad=\frac{1-e^{-j\omega\Delta t}}{\Delta t}\left(1+\frac{1+e^{-i2\omega\Delta t}-2e^{-i\omega\Delta t}}{\omega_0^2(\Delta t)^2}\right)\\
&\qquad\times\Psi_{H_z,x}|^{n+.5,\omega}_{i,j+.5,k}-\sigma_x(i)(\Delta r)^2\\
&\qquad\times\left(\frac{e^{-jk_y\Delta y}+e^{jk_y\Delta y}-2}{(\Delta y)^2}\Psi_{H_z,x}|^{n+.5,\omega}_{i,j+.5,k}\right.\\
&\qquad\quad+4\frac{1+e^{-i2\omega\Delta t}-2e^{-i\omega\Delta t}}{\omega_c^2(\Delta t)^2}\\
&\qquad\quad\times\left[\frac{\Psi_{H_z,x}|^{n+.5,\omega}_{i+1,j+.5,k}}{\kappa^2(\Delta x)^2}\right.\\
&\qquad\qquad+\frac{\Psi_{H_z,x}|^{n+.5,\omega}_{i-1,j+.5,k}-2\Psi_{Hz_x}|^{n+.5,\omega}_{i,j+.5,k}}{\kappa^2(\Delta x)^2}\\
&\qquad\qquad\left.\left.+\frac{e^{-jk_y\Delta y}+e^{jk_y\Delta y}-2}{(\Delta y)^2}\Psi_{H_z,x}|^{n+.5,\omega}_{i,j+.5,k}\right]\right) \qquad (15)
\end{aligned}$$

where Δr is simply a normalizing factor we usually set equal to Δx. This procedure would then be applied in the same manner to all the other PML terms in (25), (27), and (28) from [11]. Once again, we have simply substituted for the CCO-PML equations with the KPML equations in the calculation of the reflection coefficient. This substitution allows us to not only quantify the performance of the KPML but to also optimize it. Numerically solving the reflection coefficient is described in [11].

IV. Numerical Results

For some numerical tests we represent the PML attenuation factor, $\sigma_x(i)$ as

$$\sigma_x(i)\Delta t=\sigma_{\max}\Delta t\left(\frac{i-.5}{T}\right)^m \qquad (16)$$

where T is the PML thickness in cells and $\sigma_x(i)$ is nonzero for $i\geq 1$, i.e., our PML exists at $i\geq 1$. Let $D=[\sigma_{\max}\Delta t, m]$ then $D=[1.5,2]$ simply means that $\sigma_x(i)\Delta t=1.5((i-.5)/T)^2$. For some numerical tests we use a Gaussian PML attenuation profile defined as

$$\sigma_x(i)\Delta t=\sigma_{\max}\Delta t e^{-\left(b\frac{(i-T-1)}{4T}\right)^2} \qquad (17)$$

and the Gaussian profile is represented as $G=[\sigma_{\max}\Delta t, b]$. When specifying the evanescent term $\kappa(i)$ for ease of implementation, from [11] we have $1/\kappa(i)=1-b_0(i)$ where

$$b_0(i)=b_{0\max}\left(\frac{i-.5}{T}\right)^p \qquad (18)$$

where the evanescent profile will simply be represented by $B_0=[b_{0\max},p]$.

A. Free Space and Free Space Waveguide

We first apply the KPML to familiar situations, i.e., free-space propagation and the free-space-filled waveguide, as a reality check before we apply it to a magnetized plasma. For both cases the FDTD spaces have $\Delta x=\Delta y=\Delta z=30$ m and $\Delta t=\Delta x/\sqrt{3}c$. For a given

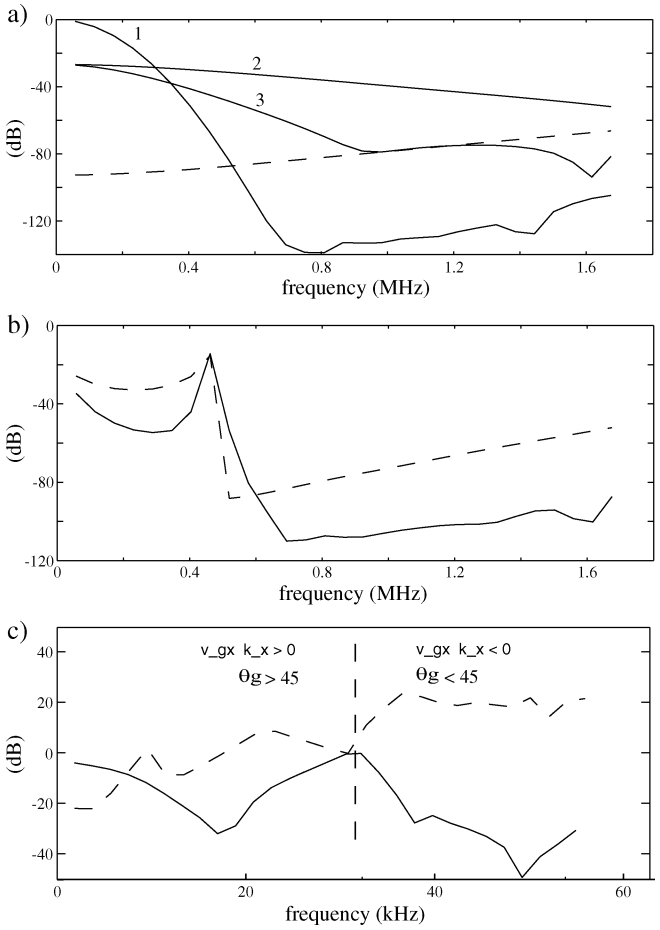

Fig. 2. (a) Freespace reflection coefficients: curve 1: $f(\omega,k_{x_{\rm pml}},k_y)=k_y^2$, curve 2: $f(\omega,k_{x_{\rm pml}},k_y)=k_{x_{\rm pml}}^2$, curve 3: $f(\omega,k_{x_{\rm pml}},k_y)=k_{x_{\rm pml}}^2+k_y^2$, dashed curve: convolutional PML. (b) freespace waveguide reflection coefficients (N = 2 mode): solid curve (KPML), dashed curve (convolutional PML). (c) magnetized plasma reflection coefficients (incident angle: 45 degrees): solid curve (KPML), dashed curve (convolutional PML).

PML attenuation profile we calculate the reflection coefficient. For both the free-space and the free-space-filled waveguide, our profile is $D=[15.5,2.0]$, which is not an optimized attenuation profile and is in fact not meant to be. We apply no evanescent attenuation, i.e. $\kappa(i)=1.0$, $B_0=[0,0]$. The PML thickness is $T=15$ cells. Fig. 2(a) plots the reflection coefficient for a few different functions of $f(\omega,k_{x_{\rm pml}},k_y)$. When $f(\omega,k_{x_{\rm pml}},k_y)=k_y^2$, the curve labeled 1, we get poor low frequency response and excellent response at higher frequencies, as expected mathematically since k_y is always real and increases with frequency. When $f(\omega,k_{x_{\rm pml}},k_y)=k_{x_{\rm pml}}^2$, the curve labeled 2, the reflection coefficient ranges between -30 to -50 dB. This performance is not very good, but since we know that $k_{x_{\rm pml}}$ is complex within the PML we do not expect outstanding performance; nevertheless, we see that the formulation does work. For $f(\omega,k_{x_{\rm pml}},k_y)=k_{x_{\rm pml}}^2+k_y^2$, we find about the average of the two previous results. Finally, the dashed line represents the traditional PML, $f(\omega,k_{x_{\rm pml}},k_y)=1.0$, using the same attenuation profile and calculated using the convolutional PML method. The convolutional PML performs the best overall.

We next calculate the reflection coefficient for the $N=2$ mode of a 2-D free-space-filled waveguide whose width is 20 cells. Fig. 2(b) plots the reflection coefficient for the convolutional PML (dashed line) and for $f(\omega,k_{x_{\rm pml}},k_y)=k_y^2=sin(2\pi/20)^2$ (solid line). The KPML and the convolutional PML perform similarly.

In addition, we obtained numerical results from both explicit and implicit time domain simulations. For the explicit simulations we apply standard Yee cell FDTD with the explicit implementation of (9). For the implicit time domain simulations we use a 2-D fully implicit FDTD electromagnetic solver that applies the single diagonally implicit Runge Kutta methods (SDIRK) [14], [15]. These fully implicit methods are unconditionally stable and provide accurate integration for stiff systems of equations. We performed time domain tests with both the KPML and the convolutional PML coexisting within the space for a free-space grid and found the simulations to be stable over time for 20,000 timesteps for both the explicit and implicit simulations. We have demonstrated that these KPML functions work as absorbing boundary conditions, not as well for open free-space problems as the traditional PML, but reasonably well for the free-space-filled waveguide.

B. Magnetized Plasma

We now apply the KPML to whistler mode waves in a magnetized plasma for which we expect it to perform better than the convolutional PML. For the reflection coefficient calculations and the explicit simulation we use an adapted version of [13] with the only modification being that we have collocated the vector electric currents with the electric fields on the FDTD grid. The properties of the magnetoplasma considered herein are the electron density, $N_e = 2 \times 10^9$ el/m^3, and the ambient magnetic field, $\hat{B}_0 = 3 \times 10^{-6}\hat{y}$ Tesla. The FDTD spaces have $\Delta x = \Delta y = \Delta z = 20$ m and $\Delta t = \Delta x/\sqrt{3}c$. The PML attenuation profile is Gaussian with $G = [.15, 6.0]$ with a thickness $T = 20$ cells. For the KPML we also apply an evanescent attenuation profile where $B_0 = [0.9, 3]$.

Fig. 2(c) plots the reflection coefficient for the convolutional PML (dashed line) and the KPML applying (4). The incident angle of the wave is 45 degrees for $v_{gx}k_x > 0$ and 45 + 180 degrees for $v_{gx}k_x < 0$. The incident power and reflected power are used to calculate the reflection coefficient; typically we use just the reflected magnetic field to calculate the reflection coefficient. We use power (instead of field components) for the magnetized plasma since Snell's law requires two reflected waves (with different phase velocities) and that therefore the power of each of the two reflected wave must be calculated and summed for a true representation of the reflected wave energy. The region to the left of the vertical dashed line in the plot [Fig. 2(c)] represents where the incident wave has $v_{gx}k_x > 0$ while that to the right represents where it has $v_{gx}k_x < 0$. It is on the right side where we expect the KPML to outperform the convolutional PML and we see that it does indeed do substantially better. As expected, the wave energy grows within the PML region for the case of the convolutional PML while the KPML attenuates the waves up to -40 dB. Even at the lower frequencies, where the incident wave has $v_{gx}k_x > 0$, the KPML performs better and attenuates all waves while the convolutional PML shows some amplification. This is because even for an incident wave with, $v_{gx}k_x > 0$, one of the two reflected waves at the PEC boundary can have $v_{gx}k_x < 0$ and thus would amplify within the convolutional PML. Also, one sees that the KPML reflection coefficient goes to zero at the frequency corresponding to $\theta_g = 45$ degrees, i.e., when θ_g equals the incident wave angle. This is by design since $f(\cdot) \to 0$ when this occurs. This is not a problem since at this angle there is no energy entering the PML, it directed in the $\hat{y}$ direction along the ambient magnetic field.

Next we perform time domain FDTD simulations for the space shown in Fig. 3(a). Once again we apply the explicit and implicit codes described in Section IV-A. We use a 20 × 20 cell space adjacent to a 20 cell PML and excite the fields with a 1 cell E_x source in the center of the space using a modulated Gaussian centered at 40 kHz with a bandwidth of 20 kHz. From (9) we set our adjustable parameter $\omega_0 = \sqrt{(\omega_c\omega_p)}$. Additionally, another mode near the

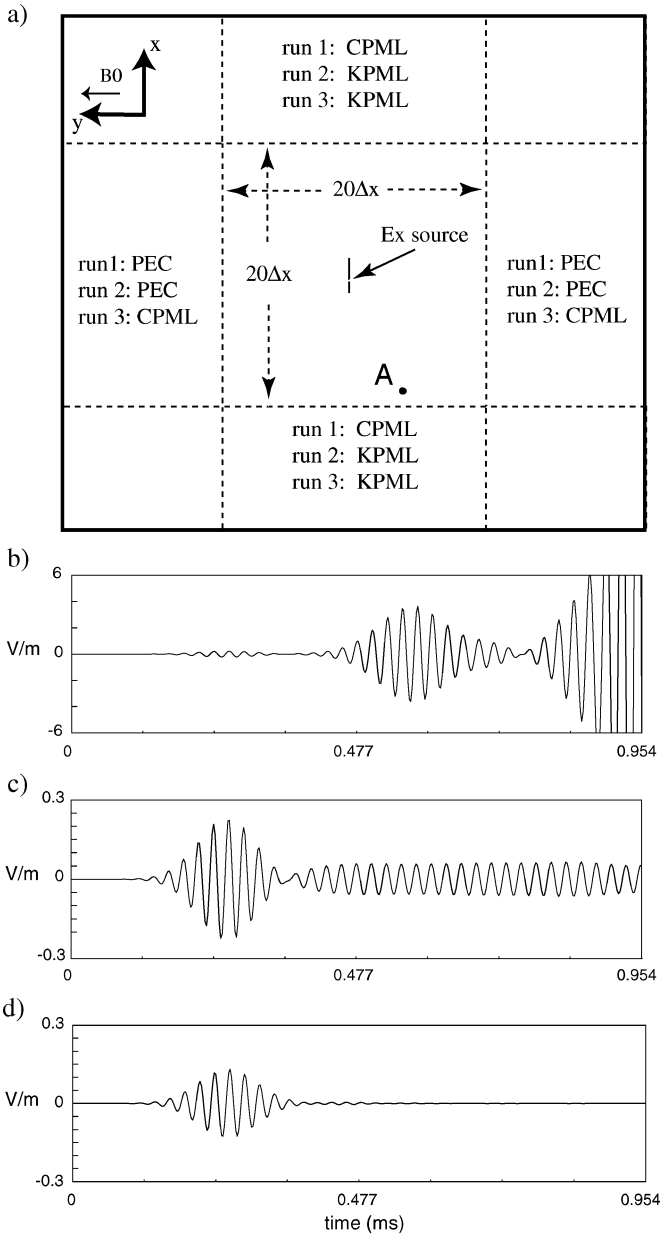

Fig. 3. (a) FDTD space for the magnetized plasma. (b)–(d) $\hat{x}$ directed electric field at point "A" over time for run 1, run 2, and run 3, respectively.

plasma frequency of the system is amplified by the convolutional PML in the $\hat{y}$-direction [8]. We apply a first order lowpass filter, [16], to the electric and magnetic fields to remove the wave energy near and above the plasma frequency to suppress the wave growth. The lowpass filter does little to the whistler mode since its frequencies are at least an order of magnitude in frequency below the plasma frequency. We compare results for three different simulations; run 1: with the convolutional PML in the $\hat{x}$-direction and PEC in the $\hat{y}$-direction, and run 2: with the KPML in the $\hat{x}$-direction and PEC in the $\hat{y}$-direction, and run 3: with the KPML in the $\hat{x}$-direction and the convolutional PML in the $\hat{y}$-direction. For all simulations we measured the $\hat{x}$-directed electric field at point "A" in the grid over time. The results of the first simulation are plotted in Fig. 3(b); we see reflected waves amplified due to the convolutional PML as expected. For the second simulation, plotted in Fig. 3(c), we see that the KPML remains stable, however there is still energy that is ringing around due to wave power that is directed in the $\hat{y}$-direction which the KPML is not designed to absorb. The third simulation has both the KPML and the convolutional PML

coexisting in the grid. The results of the third simulation are plotted in Fig. 3(d). Here we see the field over time converge to zero as all waves are now being absorbed by both PMLs. Just as important is that the system remain stable for having both types of PMLs within the space. Simulations were run for 12,000 timesteps at the courant for the implicit code. We ran the simulations for the explicit FDTD code for 16,000 timesteps at .7 of the courant. Both codes yield similar results, however, only the explicit results are plotted. It should be noted, at least in the explicit code, that for this simulation if we set $\sigma_{\max}\Delta t > 5.0$ the KPML becomes unstable, absorbing the short wavelength incident whistler waves but exhibiting growth in long wavelength waves of the same frequency and eventually saturating the entire space. Therefore, in this case the, the KPML breaks down as an absorbing boundary condition and consequently one must be careful in their choice of $\sigma_{\max}\Delta t$. However, for the free space case of Section IV-A, we found the KPML to be stable for all values of $\sigma_{\max}\Delta t$ so it really depends on the medium that the KPML is matching.

V. Summary

We have developed a new PML formulation, referred to as the KPML, which explicitly takes into account information on the k-vector direction of incident waves. The use of the KPML method is necessitated for media when the k-vector and group velocity vector components normal to the PML are antiparallel, in which case the traditional PML algorithms result in the growth of the waves (rather than their attenuation) within the PML region. We applied the KPML method to the specific case of whistler mode waves in a magnetized plasma and quantified its effectiveness with both reflection coefficient calculations as well as demonstrating the stability of the formulation with time domain simulations. The time domain results were obtained using both explicit and implicit schemes. We are currently investigating methods for optimizing the numerical reflection coefficient of the KPML as well as ways to generalize the KPML method for any anistropic medium whose k-vector and group velocity vectors differ.

Acknowledgment

We thank Dr. Tim Bell for useful discussions.

References

[1] J. P. Berenger, "A perfectly matched layer for the absorption of electromagnetic waves," *J. Computational Phys.*, vol. 114, pp. 185–200, 1994.

[2] W. C. Chew and W. H. Weedon, "A 3-D perfectly matched medium fom modified Maxwell's equations with stretched coordinates," *Micro. Opt. Tech. Lett.*, vol. 7, no. 13, pp. 599–604, Sep. 1994.

[3] V. G. Veselago, "Electrodynamics of substances with simultaneous negative values of ϵ and μ," *Sov. Phys. Usp.*, vol. 10, p. 509, 1968.

[4] G. V. Eleftheriades and K. G. Balmain, *Negative-Refraction Metamaterials*. Piscataway/Hoboken, NJ: IEEE Press/Wiley, 2005.

[5] E. Becache, S. Fauqueux, and P. Joly, "Stability of perfectly matched layers, group velocities, and anisotropic waves," *J. Computational Phys.*, vol. 188, pp. 399–433, 2003.

[6] S. A. Cummer, "Perfectly matched layer behavior in negative refractive index materials," *IEEE Antennas Wireless Propag. Lett.*, vol. 44, no. 12, pp. 1630–1639, Dec. 2005.

[7] ——, "A simple, nearly perfectly matched layer for general electromagnetic media," *IEEE Microw. Wireless Compon. Lett.*, vol. 13, no. 3, pp. 128–130, Mar. 2003.

[8] T. W. Chevalier, U. S. Inan, and T. F. Bell, "Numerical simulation of electric dipole antennas in the inner magnetosphere," presented at the URSI/Radio Science Conf., Boulder, CO, 2006, unpublished.

[9] R. A. Helliwell, *Whistlers and Related Ionospheric Phenomena*. Stanford, CA: Stanford Univ. Press, 1965.

[10] R. Gendrin, "Le guidage des whistlers par le champ magnetique," *Planet. Space Sce.*, vol. 5, pp. 274–282, 1961.

[11] M. W. Chevalier and U. S. Inan, "A PML using a convolutional curl operator and a numerical reflection coefficient for general linear media," *IEEE Trans. Antennas Propag.*, vol. 2, no. 7, pp. 1647–1657, Jul. 2004.

[12] J. A. Roden and S. D. Gedney, "Convolutional PML (CPML): an efficient FDTD implementation of the CFS-PML for arbitrary media," *Microwave Opt. Technol. Lett.*, vol. 27, no. 5, pp. 334–339, 2000.

[13] J. H. Lee and D. K. Kalluri, "Three-dimensional FDTD simulation of electromagnetic wave transformation in a dynamic inhomogeneous magnetized plasma," *IEEE Trans. Antennas Propag.*, vol. 47, no. 7, pp. 1146–1151, Sep. 1999.

[14] E. Hairer, S. P. Nørsett, and G. Wanner, *Solving Ordinary Differential Equations I: Nonstiff Problems*. New York: Springer-Verlag, 2000.

[15] ——, *Solving Ordinary Differential Equations II: Stiff and Differential-Algebraic Problems*. New York: Springer-Verlag, 2002.

[16] M. S. Sarto and A. Scarlatti, "Suppression of late-time instabilities in 3-D-FDTD analyses by combining digital filtering techniques and efficient boundary conditions," *IEEE Trans. Magn.*, vol. 37, p. 3273, 2001.

Application of Matrix Pencil to Obtain the Current Modes on Electrically Large Bodies

M. Felipe Cátedra, Fernando Rivas, Carlos Delgado, José M. Gómez, and Lorena Lozano

***Abstract*—The matrix pencil method, in combination with an interpolation using nonuniform rational bi-spline surfaces, is applied for the expansion of the induced currents on complex bodies in terms of current-modes. The approach is useful for solving electrically large problems of radiation or scattering using physical optics with one or more bounces. The techniques presented in this paper can be also useful to improve some rigorous methods.**

***Index Terms*—Electromagnetic analysis, electromagnetic scattering, parameter estimation, physical optics (PO), radar cross sections, spline functions.**

I. Introduction

Recently, several efficient methods have been developed for the rigorous numerical analysis of radiation and scattering of electrically large problems. The multilevel fast multipole algorithm (MLFMA) has improved the efficiency of the methods based on the solution of an integral equation (IE), [1]. This algorithm makes it unnecessary to compute or store the large and dense impedance matrix that appears when the IE is discretized; furthermore the CPU-time required to evaluate the application of the discretized IE operator to a vector is proportional to $N \log N$, where N is the number of samples. When an iterative method is employed to solve the discretized IE, both the CPU-time and the computer memory needed are only proportional to $N \log N$, which is a great improvement on the efficiency of the numerical method. However, N is proportional to the surface size expressed in terms of squared lambda. Typically a sampling rate in the range of 6 to 10 samples per wavelength is needed. Therefore, due to the dependence of N on the

Manuscript received August 27, 2003; revised January 27, 2006. This work was supported in part by the Spanish Department of Education and Science under Project TEC 2004-03187 and in part by the Madrid Community Project S-0505/TIC/0255.

M. F. Cátedra, C. Delgado, J. M. Gómez, and L. Lozano are with the Departamento de Ciencias de la Computación, Universidad de Alcalá, 28806 Alcalá de Henares (Madrid), Spain (e-mail: felipe.catedra@uah.es).

F. Rivas is with the Departamento de Ingeniería Electrónica de Telecomunicación y Automática, EPS de Linares, Universidad de Jaén, Linares E-23700, Spain.

Digital Object Identifier 10.1109/TAP.2006.879214